Descriptor-based method combined with partition to reconstruct three-dimensional complex microstructures

Yilin Li,[1] Shujian Chen,[2] Wenhui Duan,[3] and Wenyi Yan[1,*]

[1]*Department of Mechanical and Aerospace Engineering, Monash University, Clayton, VIC 3800, Australia*

[2]*School of Civil Engineering, The University of Queensland, St. Lucia, QLD 4072, Australia*

[3]*Department of Civil Engineering, Monash University, Clayton, VIC 3800, Australia*

(Received 10 January 2021; accepted 14 July 2021; published 30 July 2021)

A descriptor-based method combined with a partition approach is proposed to reconstruct three-dimensional (3D) microstructures based on a set of two-dimensional (2D) scanning electron microscopy (SEM) images. The features in the SEM images are identified and partitioned into small features using the watershed algorithm. The watershed algorithm first finds the local gray-level maxima, and partitions the features through the gray-level local minima. The 3D size distribution and radial distribution of the small spherical elements are inferred, respectively, based on the 2D size distribution and radial distribution using stereological analysis. The 3D microstructures are reconstructed by matching the inferred size distribution and radial distribution through a simulated annealing-based procedure. Combining with the proposed partition approach, the descriptor-based method can be applied to complex microstructures and the computational efficiency of the reconstruction can be largely improved. A case study is presented using a set of 2D SEM images with nanoscale pore structure from the low-density CSH (calcium silicate hydrate) phase of a hardened cement paste. Cross sections were randomly selected from the reconstructed 3D microstructure and compared with the original SEM images using the pore descriptors and the two-point correlation function with satisfactory agreement. Using the 3D reconstructed model, the properties of the sample material can be investigated on such a small scale as demonstrated in this paper on quantifying the absolute permeability.

DOI: 10.1103/PhysRevE.104.015316

I. INTRODUCTION

Microstructure characterization and reconstruction have been widely applied to investigate the properties of heterogeneous materials. Microstructure characterization describes the material systems statistically with statistical functions or descriptors. Microstructure reconstruction builds virtual models statistically equivalent to microstructures of the material systems [1]. With the microstructure characterization and reconstruction, the material microstructures can be investigated quantitatively, the properties of materials can be predicted using numerical simulations, and the structure-property relationships of material systems can be built. Several methods including the statistical correlation function method, descriptor-based method, and machine learning method have all been successfully applied to characterize and reconstruct the microstructures of material systems.

The statistical correlation function method uses statistical correlation functions such as the two-point correlation function, lineal-path function, and two-point cluster function to characterize the microstructure information from sample images and reconstruct the microstructure models by matching the characterized correlation functions. The two-point correlation function $S_2(r)$ measures the probability of finding two points in the same phase. The lineal-path function $L(r)$ describes the probability that an entire line with length r lies in the same phase and the two-point cluster function $C_2(\mathrm{r})$ measures the probability of finding two points with distance r in the same cluster [2]. Using these correlation functions, statistically equivalent three-dimensional (3D) microstructures can be reconstructed based on the two-dimensional (2D) sample images. The 3D microstructure reconstruction using the statistical correlation function method normally assumes that the 3D correlation functions are the same as the corresponding 2D correlation functions characterized from the sample images. After that, the voxels will be swapped based on optimization procedures to match the target correlation functions [3,4]. It has been reported by using certain correlation functions that the reconstructed 3D microstructure can reach sufficient accuracy. Yeong and Torquato used the two-point probability function and lineal-path function measured from 2D images to reconstruct the 3D microstructure of a Fontainebleau sandstone, and the 3D properties including specific surface area, pore size distribution, and permeability can be evaluated accurately from the reconstructed pore structures [5,6]. Guo *et al.* used the Yeong-Torquato procedure and the dilation-erosion method to reconstruct 3D microstructures of austenitic-ferritic cast duplex stainless steel with a percolating filamentary ferrite phase. The two-point correlation function characterized from 2D images is used for the reconstruction, and it can reach the same level of accuracy with the case considering 3D correlation functions [7]. Sumanasooriya *et al.* used the two-point correlation function method to reconstruct 3D pore structures of concrete from planar images [8]. Pore

*wenyi.yan@monash.edu

structure features and permeability were estimated based on the reconstructed 3D pore structures and the results agreed well with the experimental results. However, one critical issue of the statistical correlation function method is that during the procedure of matching objective correlation functions, pixels or voxels of the microstructure need to be swapped constantly to transform the configuration from "high energy" to "low energy", which leads to high computational cost [9]. Speeding-up techniques have been proposed to reduce the computational time, such as an adaptive schedule to achieve high cooling speed, swapping the pixels or voxels at the two-phase interface [10,11], the different-phase-neighbor based pixel selection approach [12,13], and the hierarchical annealing method with rescale of the correlation functions [14]. However, even with these techniques, the work still focuses on the permutation of pixels or voxels, and this requires a noncheap computational cost. Additionally, the microstructure is characterized by higher-order dimensional correlation functions. Although the correlation functions can contain the information of microstructure characters such as volume fraction or specific surface area, and the correlation function can be linked to the effective properties with rigorous bounds, it does not link the properties directly to the low-dimensional, physically meaningful descriptors, such as the volume fraction, pore size distribution, or other geometrical descriptors. Therefore, comparing with the descriptor-based microstructure characterization and reconstruction method, the statistical correlation function method is less suitable to analyze the structure-property relationship [1,15,16].

The machine learning method uses microstructure images to train the machine learning models and uses the trained models to reconstruct statistically equivalent microstructure samples [17]. The stochastic microstructures can be learned and reconstructed with relatively low computational cost. The machine method can also achieve the reconstruction of a 3D model based on 2D section image samples. Deep learning based generative adversarial networks (GANs) have been trained and used to reconstruct 3D microstructure based on 2D image samples [18,19].

The descriptor-based method uses physically meaningful descriptors to characterize the microstructures, and reconstruct microstructure models by matching the target descriptors stochastically. The descriptor-based method enables high computational efficiency and physically meaningful, low-dimensional microstructure characterization compared with other microstructure reconstruction methods [1,20]. Physical descriptors used for microstructure characterization and reconstruction include volume fraction; spatial descriptors such as radial distribution functions; and shape descriptors such as size distribution, aspect ratio, and roundness. The 2D and 3D relationships of these descriptors can be investigated with stereological analysis, and 3D descriptors can be inferred from the corresponding 2D descriptors. This enables the 3D microstructure reconstruction with 2D image samples. Compared with the correlation function method, the descriptor-based method focuses on matching the descriptors of objects rather than every pixel or voxel of the microstructure, which can highly increase the computational efficiency. The microstructure features are characterized using physically meaningful descriptors, which provide the potential to build the structure-properties relationship and design of the microstructure [15,16].

The advantages of the descriptor-based method are obvious when characterizing and reconstructing regular microstructures with regular features, such as voids or reinforcing particles. However, considering some complex microstructures, such as the microstructures of porous materials, the direct application of the descriptor-based method will have some limitations. The pore features in the porous materials are highly irregular, highly tortuous, and well connected, which is difficult to characterize with a few descriptors. Adding more descriptors means increasing the complexity of reconstruction and increasing the computational cost. The 2D and 3D relationships of some descriptors such as connectivity, tortuosity, and aspect ratio are difficult or impossible to investigate. These limitations restrict the application of the descriptor-based method on some complex microstructures such as the microstructure of porous materials.

In this study, a partition approach is proposed to combine with the descriptor-based microstructure reconstruction method to reconstruct 3D complex microstructures. The objective is to reconstruct 3D microstructures statistically equivalent to the information from 2D images. The 2D information can be characterized from one single image sample or a set of image samples. Using a set of image samples is intended to improve the representativity and accuracy of the data. The 3D microstructure information can be characterized and the material properties can be investigated using the 3D reconstructed model. Compared with the previous work using the descriptor-based microstructure reconstruction method directly in the literature, the proposed method partitions the original features into small features first. In this way, the partition approach can capture the irregularity, tortuosity, and connectivity of complex pore structure in porous materials and achieve high computational efficiency with the descriptor-based method. The proposed method can be applied to reconstruct 3D irregular microstructures of materials under the scale of which only 2D images can be characterized with sufficient resolution.

Circles or spheres have been successfully used as the basic elements to reconstruct the microstructure of composites or porous materials. Random sphere packing has been involved in the Laguerre-Voronoi tessellation method, which has been used to generate the microstructure of open-cell foams [21,22]. Sphere packing has also been used to reconstruct the microstructures directly. Steriotis *et al.* [23] used random sphere packing to reconstruct the digital representation of silica gel. Stiapis *et al.* [24] proposed the method starting from a random spatial distribution of spheres, then expanding and moving the spheres to nonoverlapping or partially overlapping spheres, to reconstructing the Ti2AlC ceramic foams. Thovert and Adler have proposed a method using polydisperse spheres to generate the pore structure of sandstone, with the probability density of sphere radii derived from the two-point correlation function measured on a 2D thin section [25,26]. These applications of the sphere packing method have considered the genesis of the material. For example, silica gel was considered as the agglomeration of silica microspheres and the sedimentary rock was considered as the deposition of grains followed by the consolidation. In

this case, the spheres were randomly located and the spatial correlations were not considered. Politis *et al.* proposed a hybrid method combining the process-based method and the statistical correlation function method. It first generates nonoverlapping spherical particles with random sequential deposition, then uses the simulated annealing method to match the statistical correlation functions characterized from 2D images [27]. Different from the process-based method, the proposed method here is a geometrical method. It does not consider the formation process of the material, and is not limited to the materials with the sphere packing by genesis. The proposed method artificially partitions the original feature into separated features. The intention of this is to achieve flexible reconstruction which can be applied to a broader range of materials. In this case, the spheres cannot be randomly inserted; the spatial correlation of the spheres needs to be quantified with the pair correlation function to recompose the integrated features. As a case study, the proposed method has been applied to reconstruct the nanopore structure from the low-density CSH (calcium silicate hydrate) phase of a hardened cement paste.

Cement and concrete are broadly used as construction materials. As porous materials, their pore structure has a close relationship with the mechanical and transport properties of cementitious materials. Different types of pores are linked to certain properties of cement pastes [28]. The compressive strength of a cement paste is significantly controlled by the porosity of its capillary pores [29]. It is also sensitive to the pore size of capillary pores ranging from 10 nm to 1 μm [30]. Transport properties will be affected more by the capillary pores ranging from 50 nm to 10 μm than other pore size ranges [31]. The effects of nanoreinforcements on the properties of cementitious materials are related to the nanopores in the microstructure. Besides the reinforcing effect, nanomaterials also improve the properties of cementitious materials by modifying the pore structures [32,33]. After adding nanomaterials, capillary pores and gel pores will decrease significantly, especially capillary pores above 50 nm [34–36]. The connectivity of capillary pores will be reduced and pore tortuosity will be increased [31,37]. With regard to the material properties, after adding nanomaterials, permeability and chloride diffusivity are reduced, compressive strength is increased, and durability is improved [31,34,35,38–42].

Several methods can be utilized to characterize the pore structures of cementitious materials including mercury intrusion porosimetry (MIP), scanning electron microscopy (SEM), and x-ray computed tomography (x-ray CT). MIP can obtain the porosity and pore size distribution of cementitious materials [30,43], but it cannot provide the direct information of pore morphology or the connectivity of pores which are critical to the transport properties. Some research suggested that the MIP method cannot provide actual pore size distribution for cement-based materials [44]. X-ray CT can obtain the 3D images of cement pore structures directly [1,45–48]. However, the resolution is insufficient to analyze the nanopore structures of cementitious materials. The low resolution will cause the underestimation of capillary porosity because it cannot cover the whole size range of capillary pores [46,49]. SEM has been widely used to characterize the microstructure of cementitious materials. The focused ion beam plus scanning electron microscopy (FIB SEM) technique has been applied to cement-based materials to obtain the 3D image [50,51]. However, the FIB SEM technique milling process can be destructive, the microscope can see below the cutting surface which makes the image segmentation difficult, and this method has a high cost and is time consuming which can limit the size of the sample [52]. By using the centrifugation-based low-melting-point metal intrusion technique (CLMI), high-resolution and contrast 2D SEM images of hardened cement paste pores can be obtained [32,53]. These images may not be perfect for accurate pore structure analysis, but compared with x-ray computed tomography and FIB SEM, the 2D SEM method can achieve higher resolution with lower cost, which is suitable to investigate the cement paste microstructure at the nanoscale. Applying the proposed descriptor-based reconstruction method combined with the partition approach, the 3D microstructure of hardened cement pastes with nanopores with descriptors statistically equivalent with real samples was reconstructed. The reconstructed microstructure enables the characterization of 3D nanopore structures of cement pastes and the estimation of properties at the nanoscale.

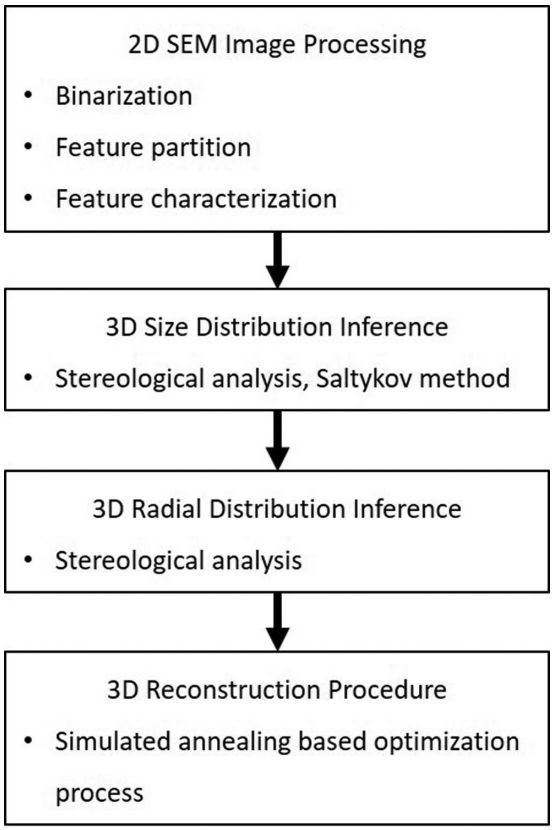

FIG. 1. Overview of the proposed reconstruction method.

II. METHOD

The overview of the proposed method is shown in Fig. 1. The method is composed of 2D image processing including the partition of the features, 3D size distribution inference, 3D radial distribution inference, and 3D microstructure reconstruction procedure. The overall concept of the proposed

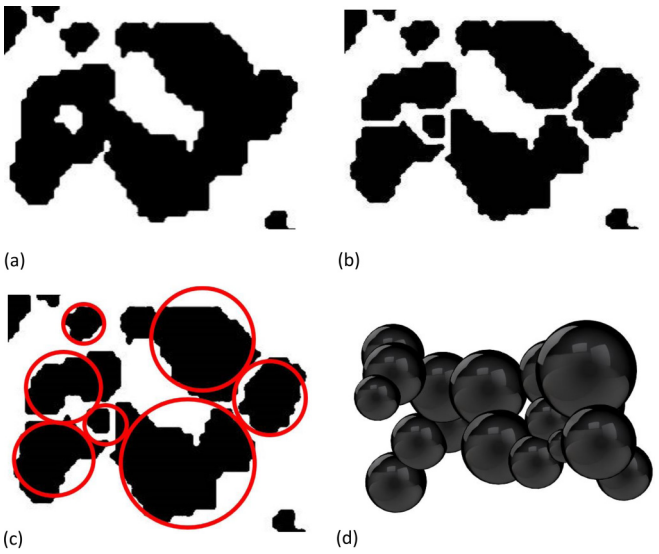

FIG. 2. Illustration of a feature reconstruction. (a) An irregular and tortuous pore in black from a 2D SEM image of a hardened cement paste. (b) The pore was partitioned into small features with the watershed algorithm. (c) The partitioned features were replaced by the circles and the pore was formed by the connected circles in 2D. (d) A 3D pore formed by connected spherical elements in 3D, which was created based on the descriptors inferred from 2D image analysis.

method is described in Sec. II A. Details of the procedure are presented in the sections after that.

A. Concept of the proposed reconstruction method

The descriptor-based method combined with a partition approach is proposed to reconstruct 3D microstructures based on the information from a set of 2D SEM images. In previous applications of the descriptor-based method on regular microstructures, the regular features, such as voids or reinforcing particles, were often treated as integrated parts [15,54]. The pore structures of porous materials such as cement pastes are highly irregular, highly tortuous, and well connected, as shown in Fig. 2(a), and are difficult to characterize as integrated parts with a few descriptors. The proposed partition approach divides the irregular pore features into small parts, as shown in Fig. 2(b). The spatial relationship of the partitioned features is evaluated statistically and used to reconstruct the 3D pore structures. This makes it easier to characterize these pore features with the small partitioned features and investigate the 2D and 3D relationship, which achieves the flexibility to reconstruct the microstructure with complex features. Furthermore, the partitioned features are much smaller and show much higher sphericity than the undivided pores. Therefore, the partitioned features are assumed to be circular in 2D and spherical in 3D, and the 3D features (pores) are formed by the connected small spherical elements, as illustrated in Figs. 2(c) and Fig. 2(d). There are two principles when performing the partition. First, the partitioned features should have high roundness. Second, the circular elements should be much larger than the size of the unit pixel or voxel. The size of the circular elements depends on the morphology of the original features. It can be indicated by the parameter roundness, which evaluates how close the shape of the partitioned feature is to a circle. In general, the partitioned features should reach satisfactory average roundness and be much larger than the size of the unit pixel or voxel. The shapes of circles and spheres are relatively simple compared with other geometries and can be fully defined only using the size descriptors. This simplifies the characterization process and the 2D and 3D relationship investigation. The connected circular and spherical elements can capture the tortuosity, irregularity, and connectivity of the cementitious material pore structure. The partitioned features are characterized through the descriptors including 2D area fraction, 2D size distribution, and 2D radial distribution. The 3D volume fraction is inferred directly from the 2D area fraction because the 2D area fraction is an unbiased estimator of the 3D volume fraction [55]. With stereological analysis, the 2D and 3D relationships of these elements are investigated and the 3D size distribution and 3D radial distribution of these spherical elements are inferred. The 3D structure is formed by these spherical elements following the inferred 3D size distribution and 3D radial distribution.

B. 2D image processing

The 2D image processing identifies the features, partitions the original features into small partitioned features, and characterizes the size and radial distribution of the partitioned features. IMAGEJ FIJI software [56] was used for 2D image processing. The SEM image of a hardened cement paste pore structure is shown in Fig. 3(a) and a 1 μm $\times$ 1 μm sample is extracted from the marked area for the demonstration. The 2D SEM image was obtained through the low-melting-point metal intrusion method, using a nontoxic Field's metal as an intrusion material to fill the pores in the cement samples. The intruded samples were polished using diamond pastes. The SEM image was taken from the cross section of the sample by the backscatter detector (BSE). The bright area represents the pores filled by the metal; the dark area represents the CSH solid. The pore phase and solid phase were first identified by applying a threshold, which processed the gray-scale images to binary images as shown in Fig. 3(b). In this process, pixels with gray level higher than the threshold were identified as the pore phase, shown as the black area in Fig. 3(b), and those lower than the threshold were defined as the solid phase, shown as the white area in Fig. 3(b). The threshold was determined by the ISODATA method [57], which calculated the average value of the integrations on the two sides of the threshold until the threshold value is equal to the average value. After the pore phase was identified, the pores were partitioned into smaller and more regular partitioned features with the watershed algorithm [58]; the partitioned features are shown in Fig. 3(c). The watershed algorithm can achieve the partition of connecting or overlapping objects automatically [59–61]. A single pore was composed of connected circles in the 2D images. The watershed algorithm first found the centers of these circles based on the local gray-level maxima. The pore objects were partitioned through the gray-level local minima between the two circle centers. When choosing the local maxima, the noise tolerance was applied. Only the

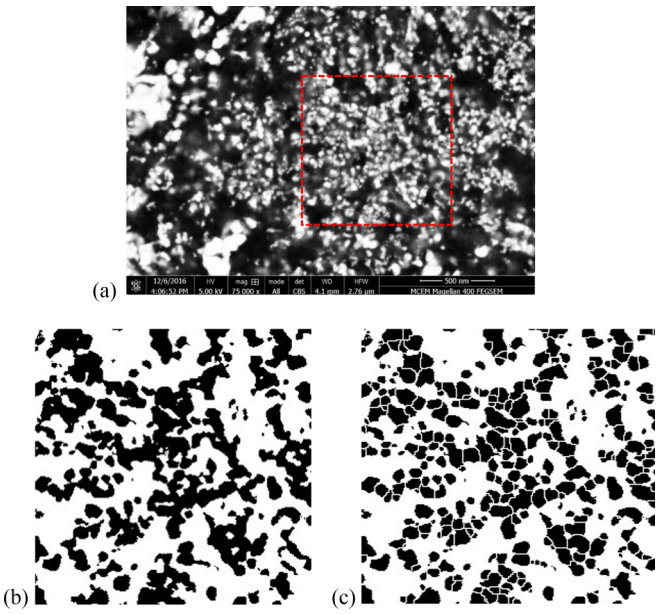

FIG. 3. (a) The SEM image of the low-density CSH phase of a hardened cement paste with nanopores obtained with the low-melting-point metal intrusion. The white area represents the pore phase, the black and gray area represents the solid phase. (b) A binarized sample image extracted from the marked area in (a) with the size 1 μm × 1 μm. The black area represents the pore phase and the white area represents the solid phase. (c) The sample image with the pore phase partitioned by the watershed algorithm.

local maxima with the gray level higher than the surrounding local maxima were preserved to prevent overpartition. The choosing of noise tolerance was based on the roundness of the partitioned features to make it closer to the circles. After finishing the partition of pores, the size distribution and radial distribution of these partitioned features were characterized. The size distribution was characterized by the equivalent circle diameter, which was the diameter of the circle with an equivalent area of the partitioned feature. The radial distribution function was used to characterize the spatial relationship of the partitioned features.

C. 3D pore size distribution inference

The 3D sphere size distribution was inferred from the characterized 2D circle size distribution using stereological analysis, the Saltykov method [62]. This method infers the 3D size distribution based on the probability of obtaining different 2D profile sizes when randomly cutting a sphere with a section [63]. This method assumes the cutting probability along the vertical axis (z) is equal; therefore, the probability of cutting at a certain vertical level z is dz/R. The relationship between the radius of the sphere R, the radius of the 2D profile r at a certain vertical level z, and the cutting level z is shown in Fig. 4(a) and in Eq. (1).

$$z(r) = \sqrt{R^2 - r^2}. \tag{1}$$

A certain range of vertical level dz can be represented by the difference of corresponding $z(r-dr)$ and $z(r)$, as shown

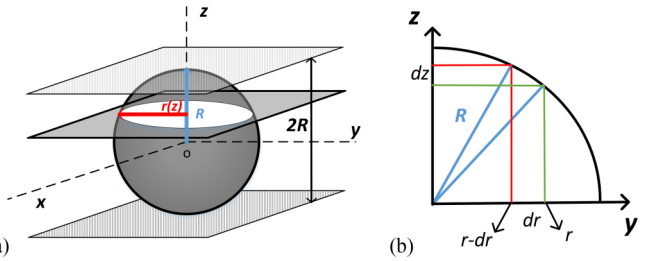

FIG. 4. (a) Illustration of a sphere cut by a plane; the red bar represents the radius of cross-section profile r at vertical level z, the blue bar is the radius of the sphere R. (b) The relationship between a certain range vertical level dz, the radius of the sphere R, and the radius of the 2D circle profile.

in Fig. 4(b) and Eq. (2) [63].

$$dz = z(r - dr) - z(r). \tag{2}$$

Combining Eqs. (1) and (2), the relationship between the vertical difference dz, the radius of the sphere R, and the radius of the 2D circle profile is [63]

$$dz = \sqrt{R^2 - (r - dr)^2} - \sqrt{R^2 - r^2}. \tag{3}$$

For a sphere with the radius R, when cutting by a section randomly, the probability of getting a 2D circle profile with the radius between $(r-dr)$ and r can be calculated by [63]

$$\Pr\{r > r_i > (r - dr)R\} = \frac{1}{R}[\sqrt{(R^2 - (r - dr)^2)} - \sqrt{(R^2 - r^2)}]. \tag{4}$$

Next, considering a group of spheres with diameter D, the relation of 3D particle number density N_V and 2D particle number density N_a is given by

$$N_a = DN_V. \tag{5}$$

The 3D particle number density N_V is the number of sphere centers per unit volume of the cube and 2D particle number density N_a is the number of profiles within the unit area of the section.

The Saltykov method assumes that the diameter of the largest sphere $D_{\max}$ is equal to the largest circle in the cross-section area. The 2D and 3D size ranges are divided into the same number of discrete identical intervals [64]. The size interval Δ is determined by the largest sphere diameter $D_{\max}$ and the number of the intervals m; i.e.,

$$\Delta = \frac{D_{\max}}{m}. \tag{6}$$

Let i be the number of size intervals in 3D and j be the number of size intervals in 2D. $N_a(j)$ is the particle number density of 2D cross-section circle profiles which are obtained from the SEM images. $P(j, i)$ is the probability of cross sections produced by 3D spheres in size interval i falling into 2D size interval j. The 2D circle profiles in the cross section can only come from the 3D spheres with a radius equal to or larger than the radius of the 2D circle profiles. Therefore, the number of 2D circle profiles in the size interval $N_a(j)$ is the summation of the product of the number of spheres in size interval i, $N_V(i)$, and the diameter of the sphere D_i,

and the probabilities of cross-sectional profiles produced by 3D spheres in this interval i fall into the 2D size interval j, $P(j, i)$; i.e., [65]

$$N_a(j) = \sum_{i=j}^{m} P(j, i) D_i N_V(i). \tag{7}$$

Based on the aforementioned stereological method, Eq. (4), the probability of obtaining 2D profiles in 2D size interval j from 3D sphere size interval i is given by [65]

$$\begin{aligned} P(j, i) &= \frac{1}{D_i}\left[\sqrt{{D_i}^2 - (d_j - \Delta)^2} - \sqrt{{D_i}^2 - {d_j}^2}\right] \\ &= \frac{1}{i}\left[\sqrt{i^2 - (j-1)^2} - \sqrt{i^2 - j^2}\right]. \end{aligned} \tag{8}$$

With the 2D profile size distribution obtained from the image processing step, the 3D size distribution of the elements can be inferred by solving the linear relationship in Eq. (7).

D. 3D radial distribution inference

The radial distribution function $g(r)$, also called the pair correlation function, describes the spatial correlation and the dispersion of elements. It is defined as the probability of finding any particle at a radial distance r from the center of another particle [66]. Rintoul and Torquato used it to reconstruct the dispersions of particles [67]. In the proposed method, the 3D radial distribution is inferred by analyzing the position relationship of two elements in 3D space based on the 2D radial distribution characterized from SEM images. The periodic boundary condition is applied for both 2D radial distribution characterization and 3D radial distribution matching to overcome the boundary effect of the sample [68]. In 2D cases, the radial distribution function $g(r)$ is the number density inside a ring with the radius r and the thickness Δr, i.e., [66]

$$\begin{aligned} g(r) &= \frac{1}{2\pi N r \rho_0} \sum_{j=1}^{N} \sum_{\substack{i=1 \\ i \neq j}}^{N} \delta(r - r_{ij}) \\ &= \frac{1}{\pi N r \rho_0} \sum_{j=1}^{N} \sum_{i>j}^{N} \delta(r - r_{ij}), \end{aligned} \tag{9}$$

where $\rho_0 = N/A$ is the average number density. N is the number of elements in the entire sample, A is the area of the sample, and δ is the Dirac delta function.

In 3D cases, radial distribution function $g(r)$ represents the number density inside a spherical shell with the radius r and the thickness Δr, i.e., [66]

$$\begin{aligned} g(r) &= \frac{1}{4\pi N r^2 \rho_0} \sum_{j=1}^{N} \sum_{\substack{i=1 \\ i \neq j}}^{N} \delta(r - r_{ij}) \\ &= \frac{1}{2\pi N r^2 \rho_0} \sum_{j=1}^{N} \sum_{i>j}^{N} \delta(r - r_{ij}), \end{aligned} \tag{10}$$

where $\rho_0 = N/V$, N is the number of elements in the entire sample, and V is the volume of the sample.

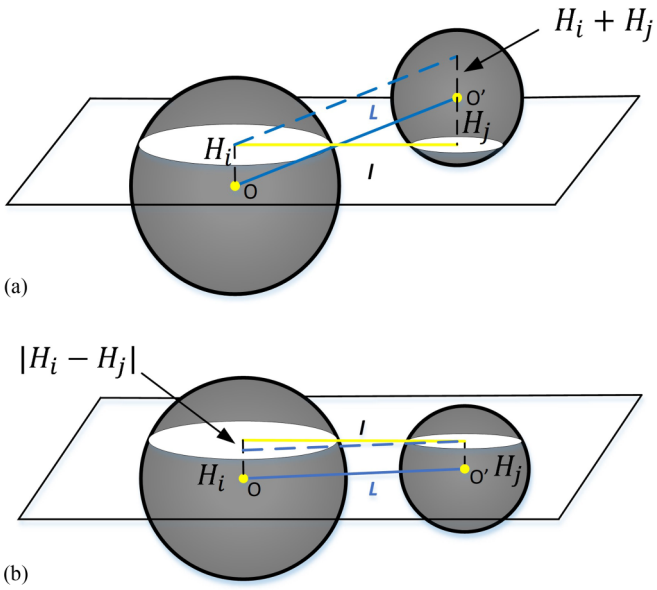

FIG. 5. Illustration of the relation of the distance between two sphere centers to the projection distance between two circle centers. (a) Two sphere centers located at the opposite side of the cutting plane. (b) Two sphere centers located at the same side of the cutting plane. The yellow line represents the projection distance l on the cutting plane between two circle centers and the blue line represents the 3D distance L between two sphere centers.

To infer the 3D radial distribution function from the 2D radial distribution function characterized from SEM images, the spatial relationship between two elements is analyzed. Two cases are considered, one where the two sphere centers are located at the opposite side of the cutting plane, as shown in Fig. 5(a), and one where the two sphere centers are located at the same side of the cutting plane, as shown in Fig. 5(b).

The distance between two circle centers seen in the 2D images is the projection of the real distance between the two spheres in 3D. As seen in Fig. 5, there may be some vertical distance between the center of the spheres and the center of the circles on the section plane. To infer the real distance between the centers of two spheres, the probabilities of obtaining different vertical distances H_i and H_j are analyzed. It is assumed that the position of the section plane is equal throughout the vertical direction, the two vertical distances for the two elements between the center of circles in the section profile and the center of spheres are independent, and there is an equal probability of having the center of the spheres in the same side of the section plane and the opposite side of the section plane.

The real distance between two sphere centers L is determined by the projected distance on section plane l, and the vertical distance H_i and H_j gives

$$L = \begin{cases} \sqrt{l^2 + (H_i + H_j)^2} \text{ (spheres on the same side)} \\ \sqrt{l^2 + |H_i - H_j|^2} \text{ (spheres on the opposite side)} \end{cases}. \tag{11}$$

The range of the vertical distance is constrained by the size of the spheres. If the vertical distance between the center of

the sphere and the section plane is larger than the radius of the sphere, there will be no cross-sectional profile shown on the section plane. Therefore, the highest possible vertical distance is the radius of the sphere. The probability of getting different vertical distance H_i and H_j is related to the radius of the spheres and the probability of the size of the spheres. Based on the assumption of equal cutting probability in the vertical direction, for a sphere with a given radius, the probability of getting a certain vertical distance H is the inverse value of the radius, i.e.,

$$P_2(H_i) = \int_{H_i}^{\mathrm{Rmax}} \frac{1}{x} P_1(x)dx, \tag{12}$$

$$P_2(H_j) = \int_{H_j}^{\mathrm{Rmax}} \frac{1}{y} P_1(y)dy, \tag{13}$$

where x and y are the radii of the two spheres, $P_1(x)$ is the probability function of the sphere radius, and $P_2(H)$ is the probability function of the vertical distance between the sphere center and the circle center on the section plane.

Assuming that it takes independent events to get two vertical distances, the probability of having H_i and H_j for the two spheres $P_3(H_i, H_j)$ is equal to the product of having the probability of vertical distance H_i and H_j.

$$\begin{aligned} P_3(H_i, H_j) &= P_2(H_i)P_2(H_j) \\ &= \int_{H_i}^{\mathrm{Rmax}} \frac{1}{x} P_1(x)dx \int_{H_j}^{\mathrm{Rmax}} \frac{1}{y} P_1(y)dy \\ &= \int_{H_j}^{\mathrm{Rmax}} \int_{H_i}^{\mathrm{Rmax}} \frac{1}{xy} P_1(x)P_1(y)dxdy. \end{aligned} \tag{14}$$

The probability function of the inferred distance between two sphere centers $P_5(L)$ is the product value of the probability of having H_i and H_j for the two spheres and l for the projected distance on the section plane. The corresponding value of L is given by

$$P_5(L) = P_3(H_i, H_j)P_4(l), \tag{15}$$

where $P_4(l)$ is the probability function of the distance between the center of two circle profiles on the section plane, which can be characterized on 2D images.

The radial distribution function is calculated based on the probability of the inferred 3D distance between sphere centers and the volume of the sample, i.e.,

$$g(r) = \frac{1}{\frac{dv}{V}} \frac{\sum_{j=1}^{N} \sum_{\substack{i=1 \\ i \neq j}}^{N} \delta(r - r_{ij})}{N^2}. \tag{16}$$

The volume of the sample is assumed to be equal to a torus with the radius r, width Δr, and height $2R_{\max}$.

In 3D cases, $P_5(L)$ is the distribution of the radial distance between two sphere centers, i.e.,

$$P_5(L) = \frac{\sum_{j=1}^{N} \sum_{\substack{i=1 \\ i \neq j}}^{N} \delta(r - r_{ij})}{N^2}. \tag{17}$$

The 3D radial distribution function can be represented by the inferred 3D probability function of the radial distance between two sphere centers $P_5(L)$ divided by the volume density of the torus; i.e.,

$$g(r) = \frac{1}{\frac{dv}{V}} P_5(L). \tag{18}$$

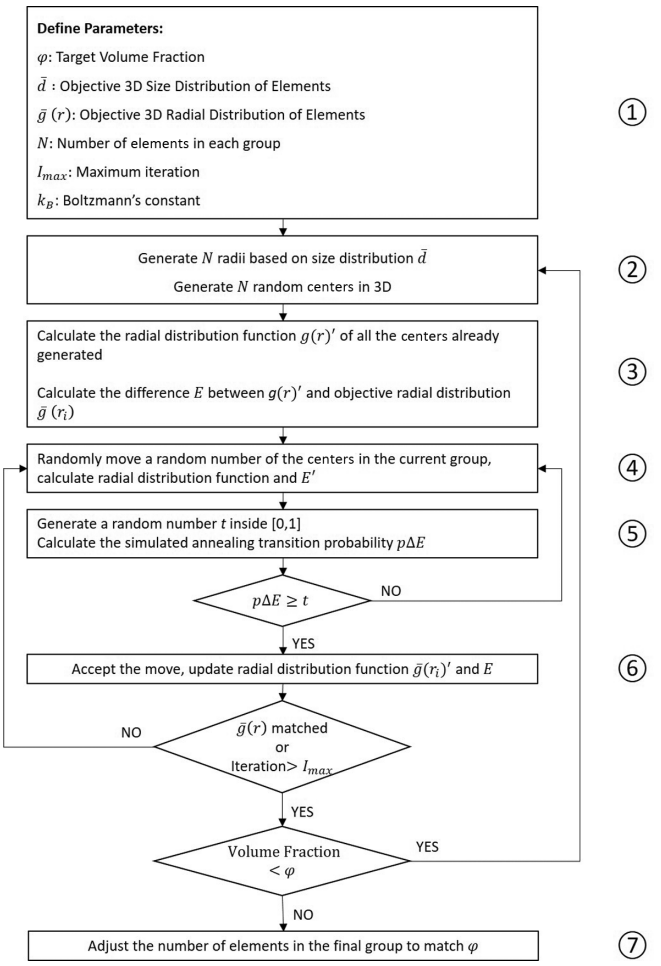

FIG. 6. Pore structure reconstruction flowchart using the inferred 3D information.

E. 3D model reconstruction procedure

The flowchart of the reconstruction procedure is shown in Fig. 6. The 3D microstructure was reconstructed stochastically by matching the volume fraction, 3D size distribution, and 3D radial distribution of the spherical elements. Firstly, the target volume fraction ϕ, element size distribution $\bar{d}$, objective radial distribution function $\bar{g}(r)$, number of elements in each group N, and maximum number of random moving iterations $I_{\max}$ were set, as shown in step 1 in Fig. 6. The elements were generated by groups. For each group, the 3D size distribution and radial distribution were matched with the objective value. Secondly, N radii were generated based on the size distribution $\bar{d}$; after that random positions for these elements were generated, as shown in step 2 in Fig. 6, and the radial distribution function $\bar{g}(r)'$ was calculated for all the centers generated. The radial distribution function was obtained by calculating the distance between every two centers of the elements, which can be time consuming. However, the calculations of the distances between the elements are

independent and do not affect each other. Therefore, parallel computing was applied which can calculate the distances between elements simultaneously. The computational load was divided into discrete tasks and allocated to different CPUs. With parallel computing, the computational time was significantly reduced.

The simulated annealing optimization procedure was applied to optimize the position of the elements to match the radial distribution. Based on the simulated annealing method, the difference E between the radial distribution function of generated elements $\bar{g}(r)'$ and the objective radial distribution function $\bar{g}(r)$ was calculated as [69]

$$E = \sum_i |\bar{g}(r)' - \bar{g}(r)|, \tag{19}$$

as shown in step 3 in Fig. 6.

The positions of some of the elements were moved randomly and the differences between the radial distribution functions were recalculated, as shown in step 4 in Fig. 6. The randomly moved positions were compared with the previous positions by calculating the energy difference ΔE; i.e.,

$$\Delta E = E' - E. \tag{20}$$

Whether the random move will be accepted or not will depend on the acceptance probability $p\Delta E$ as shown in steps 5 and 6 in Fig. 6, i.e., [67]

$$p\Delta E = \begin{cases} 1 & \Delta E \leqslant 0 \\ \exp\left[-\frac{\Delta E}{k_B T}\right] & \Delta E > 0 \end{cases}, \tag{21}$$

where k_B is the Boltzmann's constant and is set to equal 1 for simplicity; T is the temperature controlling the simulated annealing process [69].

The simulated annealing procedure can prevent the optimization from being trapped in local minima. The maximum randomly moving iteration is defined and this value will decrease as the group of elements increases. This value ensures the convergence of energy difference. It also ensures the energy difference is small enough to make the radial distribution of the reconstructed model and the target radial distribution match. If the distributions of the reconstruction model cannot match the target distributions, the maximum randomly moving iteration should be increased. After reaching the maximum randomly moving iteration, the random movement is terminated and the procedures are repeated for the next group of elements until the volume fraction of the model reaches the target volume fraction.

III. RESULTS AND DISCUSSION

As a case study, the proposed method was applied to reconstruct the microstructure of the low-density CSH phase of hardened cement pastes with nanoscale pores. Original 2D image samples with the size 1 μm $\times$ 1 μm were randomly selected from the SEM image in Fig. 3(a). The mean equivalent pore diameter was 45 nm. This sample size was chosen based on the cement paste pore size of interest. With the sample size 1 μm $\times$ 1 μm, the pores inside the range of 10–100 nm can be observed clearly. The reconstructed 3D microstructure is presented and evaluated in the following subsections.

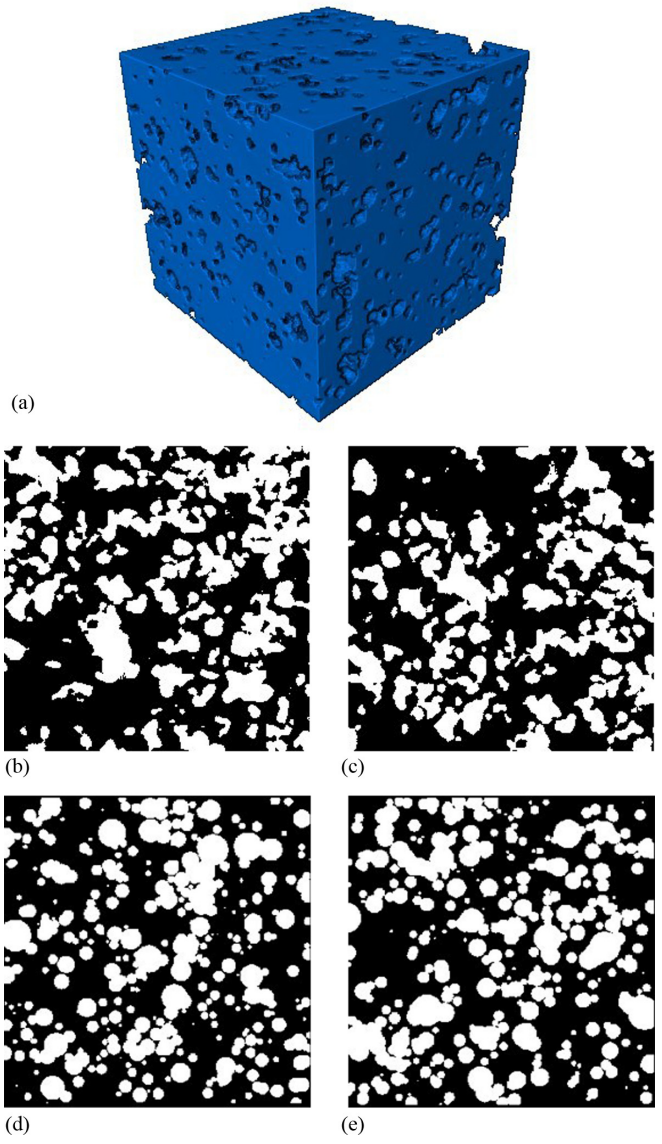

FIG. 7. (a) Reconstructed 3D model of the low-density CSH phase of a hardened cement paste with nanopores. The size of the model is 1 μm $\times$ 1 μm $\times$ 1 μm. (b),(c) Binarized original 2D image samples from the 2D SEM. (d),(e) Cross sections cut randomly from the reconstructed 3D model.

A. 3D reconstructed microstructure

The reconstructed 3D microstructure of the hardened cement pastes with nanoscale pores is shown in Fig. 7(a). The size of the model is 1 μm $\times$ 1 μm $\times$ 1 μm. The blue solid part in the model represents the solid phase of hardened cement pastes and the voids in the model are the pores. The pores are well connected in 3D space and the shapes of the pores are highly irregular and tortuous. The pores are distributed uniformly across the 3D model without overconcentration or overdispersion.

Two binarized original 2D sample images are shown in Figs. 7(b) and 7(c) and two cross sections cut randomly from the reconstructed model are shown in Figs. 7(d) and 7(e). Similar to the original images, it can be observed from Figs. 7(d) and 7(e) that large irregular and connected pores are formed

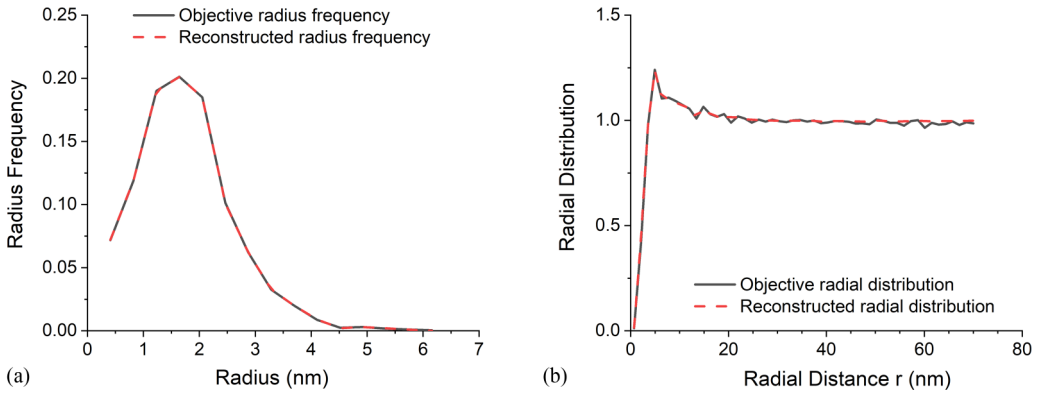

FIG. 8. (a) Comparison of element radius frequency in the reconstructed model with the objective element radius frequency. (b) Comparison of element radial distribution in the reconstructed model with the objective element radial distribution function.

in the reconstructed model. The pore profiles in the original images and cross sections from the reconstructed model show similar size and spatial distribution. As the partitioned pore features are assumed to be circular in 2D and spherical in 3D to achieve the reconstruction flexibility, when comparing in details, the reconstructed model does not match perfectly the irregularity and tortuosity of the pore profiles in the SEM image.

B. Verification of the reconstruction procedure

To verify the reconstruction procedure, the 3D size distribution and radial distribution function of the reconstructed model were compared with the objective 3D size distribution and radial distribution function, respectively, as shown in Figs. 8(a) and 8(b). Clearly, the size distribution and radial distribution function agree well with their objective functions. The maximum randomly moving iteration is enough to obtain the small and convergence results of energy difference. The reconstruction procedure can build the 3D pore structure model statistically equivalent to the objective distributions.

C. Evaluation of 3D reconstructed microstructure

To evaluate the accuracy of the reconstructed model, cross sections from the reconstructed model were randomly selected, and compared with the original SEM sample images quantitatively. Pore descriptors including equivalent pore diameter, circularity, solidity, aspect ratio, and the Skvortsova's shape factor were used to quantify the size and shape of pore profiles on 2D images. These shape factors had been applied to evaluate the shapes of soil pores or cement pores in the literature [70]. The two-point correlation function and lineal-path function were used to evaluate the pores on the 2D images.

1. Pore profile size and shape

The pore descriptors used to evaluate the pore profiles are introduced as follow. Pore profile size is described by the equivalent pore diameter d_p, which represents the diameter of a circle with the same area of the pore, given as

$$d_p = \sqrt{\frac{4A}{\pi}}, \tag{22}$$

where A is the area of the pore. Equivalent pore diameter actually is a one-dimensional descriptor of the area of the pores.

The shape of the pore profile is described by circularity, solidity, aspect ratio, and Skvortsova's shape factor. Circularity is a shape descriptor describing the relationship between the area and perimeter of the pores, given as

$$C = \frac{4\pi A}{P^2}, \tag{23}$$

where P is the perimeter of the pore cross section. The maximum value of circularity is 1, which means the pore profile is a circle. The more irregular the pore profile is, the smaller the value of circularity [28].

Solidity is another pore shape descriptor, which is defined as the ratio of the pore profile area to the corresponding convex area, given as [32]

$$S = \frac{A}{A_{\text{Convex}}}, \tag{24}$$

where A_{convex} is the convex area. Convex area refers to the area of the convex polygon which can enclose the pore profile, and all interior angles of the polygon are less than 180°. Solidity describes the density of the geometry. Solidity equal to 1 means that the geometry is fully solid. Solidity less than 1 means the boundary of the geometry is irregular or the inside of it has voids [71].

Aspect ratio (R_A) is the parameter used to describe the elongation of pores. The definition is the ratio of the major axes length to the minor axes length of the fitted ellipse, i.e. [32],

$$R_A = \frac{L_{\text{major axis}}}{L_{\text{minor axis}}}, \tag{25}$$

where $L_{\text{major axis}}$ and $L_{\text{minor axis}}$ are the lengths of the major and minor axes of the fitted ellipse. The aspect ratio of a circle is 1. A higher aspect ratio means the pore profile is elongated over a particular direction.

Skvortsova's shape factor is defined as

$$F = \left(\frac{4\pi A}{P^2} + \frac{D}{L}\right) \Big/ 2, \tag{26}$$

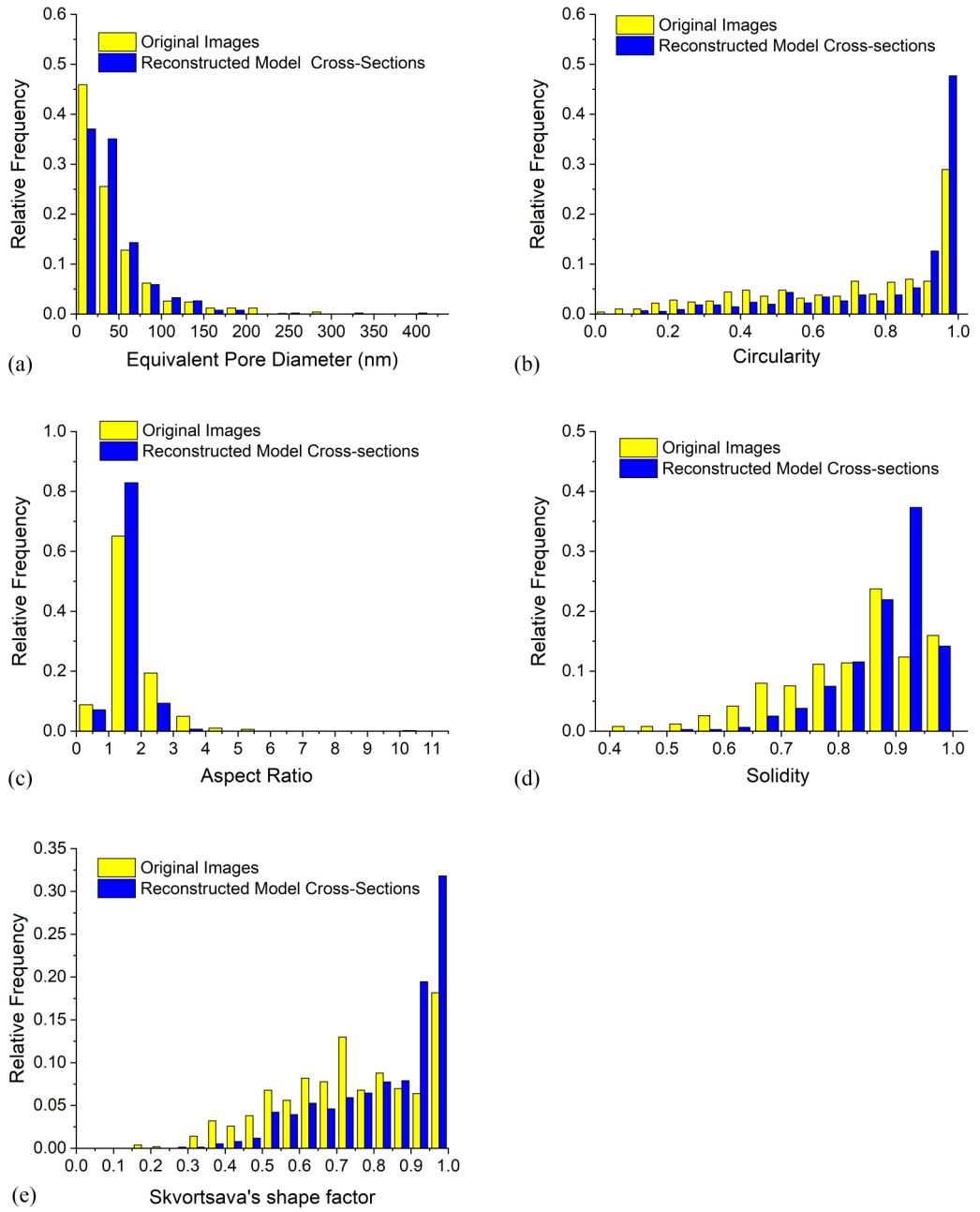

FIG. 9. (a)–(e) Comparison of pore descriptors between original images and randomly selected cross sections from the reconstruction model: (a) equivalent pore diameter; (b) circularity; (c) aspect ratio; (d) solidity; (e) Skvortsova's shape factor.

where D is the width of the circumscribing rectangle; L is the length of the circumscribing rectangle.

The Skvortsova's shape factor puts other shape factors together, with the first term reflecting the roundness of the shape and the second term reflecting the isometry of the shape. It can reflect fissurelike shapes with $F \in (0,\ 0.2)$, elongated dissected shapes with $F \in (0.21,\ 0.4)$, isometric dissected shapes with $F \in (0.41,\ 0.6)$, isometric slightly dissected shapes with $F \in (0.61,\ 0.8)$, and rounded shapes with $F \in (0.81,\ 1.0)$ [72,73].

The results of the comparisons are shown in Fig. 9. The five original sample images used for reconstruction and five randomly cut cross sections from the reconstructed model were selected. The relative frequency of the aforementioned pore descriptors from the five original sample images and the five reconstructed model cross sections were calculated and compared.

With regard to the size distributions shown in Fig. 9(a), the original images and reconstructed model cross sections both have the highest relative frequency of equivalent pore diameter in the class 0–25 nm, with the relative frequency 0.46 for the original images and 0.37 for the reconstructed model cross sections. The second highest relative frequency is the class 25–50 nm for both original images and reconstructed model cross sections, with relative frequency 0.26 for the original images and 0.35 for the reconstructed model cross sections. Concerning both cases, it shows that more than half of the pores are within the equivalent pore diameter

TABLE I. Comparison of microstructure descriptors between the original images and reconstructed model cross sections. "SD" represents standard deviation.

		Original Images	Reconstructed model cross sections	Difference
1. Porosity (%)		35.71	35.75	0%
2. Equivalent pore diameter d_p (nm)	Mean	44.85	42.08	6%
	SD	50.31	34.84	36%
3. Circularity	Mean	0.72	0.83	15%
	SD	0.27	0.22	19%
4. Solidity	Mean	0.83	0.88	7%
	SD	0.13	0.08	46%
5. Aspect Ratio	Mean	1.80	1.38	26%
	SD	0.84	0.44	63%
6. Skvortsova's shape factor	Mean	0.74	0.84	13%
	SD	0.19	0.16	17%

range smaller than 50 nm. For the following equivalent pore diameter classes from 50 to 200 nm, the original images and reconstructed model cross sections have a similar value of relative frequency. When considering large equivalent pore diameter classes above 200 nm, the original images do have a few pores falling inside these ranges, but this cannot be observed in the reconstructed model. Generally, the original images and reconstructed model cross sections show a similar size distribution pattern of pore profiles, but the original images have a few large pore profiles that cannot be observed in reconstructed model cross sections.

As shown in Fig. 9(b), the circularities of pore profiles from original images and reconstructed model cross sections have a similar pattern of distribution. Both distributions have the highest relative frequency inside the range 0.95–1, and both cases have low relative frequency inside the ranges from 0.1 to 0.9. The spread of the circularity for both cases is wide, from less than 0.2 to 1, which indicates both the original images and reconstructed model cross sections have irregular pore profiles. Compared with the pore profiles in the original images, the pore profiles in the reconstructed model cross sections have a higher relative frequency for high circularity from 0.9 to 1, which means the pore profile boundaries on reconstructed model cross sections are more regular and smoother; the pore profile boundaries in the original images are more tortuous. Overall, the circularity still shows a similar distribution for pore profiles from the original images and reconstructed model cross sections.

As shown in Fig. 9(c), the aspect ratios of pore profiles from original images and reconstructed model cross sections have a similar pattern of distribution. Both cases have the highest relative frequency in the range 1–2, with the relative frequency 0.65 for the original images and 0.83 for the reconstructed model cross sections, followed after that by the second highest range, 2–3, with the relative frequency 0.19 for original images and 0.09 for the reconstructed model cross sections. For the pore profiles with aspect ratio 1, the original images have the relative frequency 0.087 and reconstructed model cross sections have the relative frequency 0.07. Concerning both cases, over 90% of the pore profiles have the aspect ratio under 3, with no extreme elongation. However, the original images have one extreme outlier with an aspect ratio of 10. In the reconstructed model, there are no pore profiles with the aspect ratio larger than 4.

As shown in Fig. 9(d), the solidities of pore profiles for both original images and reconstructed model cross sections have a similar pattern of distribution and they are concentrated inside the range 0.8–1. They have very similar relative frequency inside the range 0.8–0.85, 0.85–0.9, and 0.95–1.0. However, the highest solidity relative frequency of the original images is in the range of 0.85–0.9, and the corresponding relative frequency of reconstructed model cross sections is in the range of 0.9–0.95. The spread of pore profile solidity is wider for the original images than the reconstructed model cross sections, which means the boundary of pore profiles in the original images is a little bit more irregular. Generally, besides the difference in solidity class 0.9–0.95, the solidity shows a similar distribution for pore profiles from the original images and reconstructed model cross sections.

As shown in Fig. 9(e), the Skvortsova's shape factor for both original images and reconstructed model cross sections has a similar pattern of distribution. Both cases have the highest relative frequency at 0.95–1, and a similar relative frequency for classes except 0.7–0.75, 0.9–0.95, and 0.95–1. For both cases, elongated dissected pores, isometric dissected pores, isometric slightly dissected pores, and rounded pores can be found. However, few fissurelike pores can be found in the original images, which are not found in the reconstructed model cross sections. The reconstructed model cross sections have more rounded pores than the original images, and the original images have more isometric, slightly dissected shape pores than the reconstructed model cross sections. Generally, a similar pattern of Skvortsova's shape factor distribution is achieved for the original images and reconstructed model cross sections.

The pore profiles of the original images and reconstructed model cross sections were compared using the mean value and standard deviation of the aforementioned descriptors, and the porosity was also compared. The results are shown in Table I. The average porosity of the original images is 35.8%, and the reconstructed model cross sections have the same average porosity of 35.8%. The mean value of equivalent pore diameter for the original images is 44.9 nm, and for the reconstructed model, it is 42.1 nm, with a difference of

6%. The standard deviation of equivalent pore diameter from the original images is 50.3 nm and the reconstructed model cross section is 34.8 nm, with a difference of 36%. It shows that the average size of pore profiles is similar comparing the original images and reconstructed model cross sections, but the original images have a wider spread of pore profile size. With regard to the shape of the pore profile, the mean values of circularity for the original images and reconstructed model cross sections are 0.72 and 0.83, for solidity they are 0.83 and 0.88, for aspect ratio they are 1.80 and 1.38, and for Skvortsava's shape factor they are 0.74 and 0.84. The standard deviations of circularity for the original images and reconstructed model cross sections are 0.27 and 0.22, for solidity they are 0.13 and 0.08, for aspect ratio they are 0.84 and 0.44, and for Skvortsava's shape factor they are 0.19 and 0.16. The mean values of the pore shape descriptors are similar comparing the original images and reconstructed model cross sections, but the standard deviations are higher for the original images, which means the original images and reconstructed model cross sections have a similar pattern in general, but the original images have more irregular pore profiles.

Generally, the comparisons of the aforementioned descriptors show similar statistical patterns, which means the reconstructed model can achieve overall statistical equivalent shape descriptors of the original SEM images. However, to achieve the flexibility of the reconstruction, the partitioned pore features are assumed to be circular in 2D and spherical in 3D. Therefore, when comparing in detail, the reconstructed model cannot achieve the same irregularity and tortuosity of pore profiles as the SEM images. Considering the objective of the reconstruction is to build pore structure models statistically equivalent to the characters on SEM images, the overall results are satisfactory.

2. Comparison with statistical correlation functions

The two-point correlation function and lineal-path function of the original images and the reconstructed model cross sections are calculated. These correlation functions are used to investigate the point to point relation of the pore phase in the original images and the reconstructed model cross sections. Two-point correlation function describes the probability of finding two points in the same phase, which focuses on the relative position between points in the pore phase. The two-point correlation function $S_2^{(i)}(\mathrm{r})$ is defined as follows,

$$S_2^{(i)}(\mathbf{r}) = S_2^{(i)}(\mathbf{x}_1, \mathbf{x}_2) = \langle I^{(i)}(\mathbf{x}_1) I^{(i)}(\mathbf{x}_2) \rangle, \tag{27}$$

where $\langle \cdots \rangle$ denotes the ensemble average, $\mathbf{r}$ represents the separation between two points defined as $\mathbf{r} = |\mathbf{x}_1 - \mathbf{x}_2|$, $I^{(i)}(x)$ is the phase characteristic function which is defined as

$$I^{(i)}(\mathrm{x}) = \begin{cases} 1, & \text{if } x \in \upsilon_i \\ 0, & \text{otherwise} \end{cases}, \tag{28}$$

where υ_i is Euclidean space with phase i [2,74].

By using the two-point correlation function, the relative positions between every two pixels of the original images and reconstructed model cross sections are evaluated.

The lineal-path function describes the probability that a line segment with length z is entirely within the same phase j in the sample [13,66]. It is an important descriptor related to the transport properties of heterogeneous materials [75]. The lineal-path function is given as

$$L^{(j)}(\mathrm{z}) = \begin{cases} (l - z)/N, & 0 \leqslant z \leqslant l \\ 0, & \text{otherwise} \end{cases}, \tag{29}$$

where N is the sample size; l is the total length of the chord.

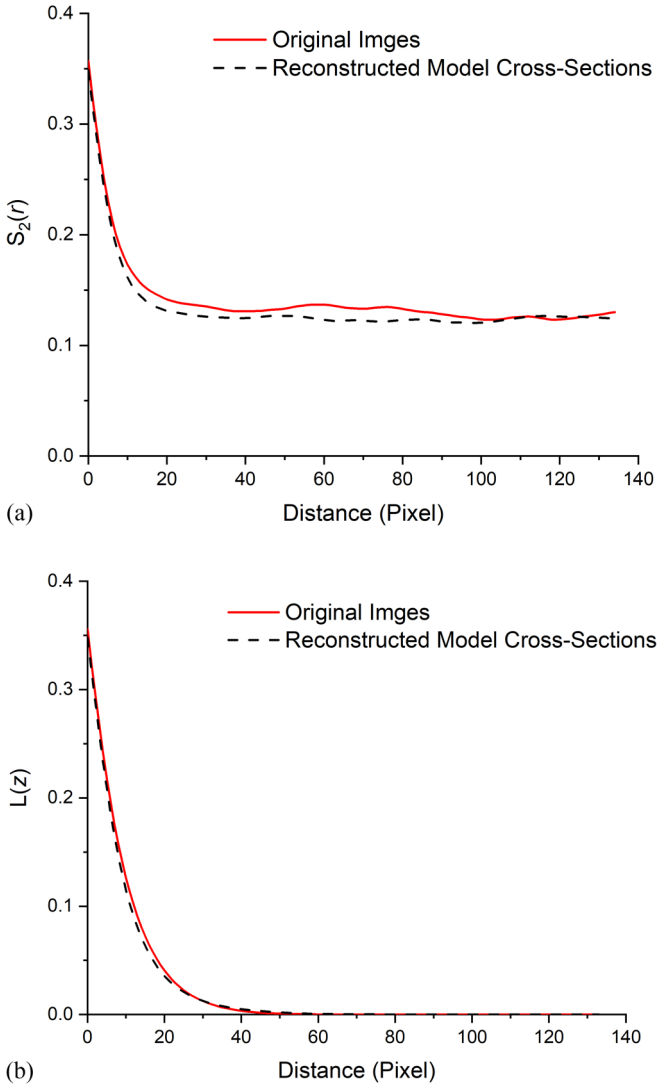

FIG. 10. Comparison of original images and reconstructed model cross sections with statistical correlation functions: (a) Two-point correlation function; (b) lineal-path function.

As shown in Figs. 10(a) and 10(b), the two-point correlation functions and lineal-path functions of the original images and reconstructed model cross sections agree well with each other, which means the reconstructed model has statistically equivalent correlation functions of the SEM images. Two-point correlation function and lineal-path function are commonly used correlation functions when reconstructing 3D microstructure using the conventional statistical correlation function method [5,13]. The match of the correlation functions can verify the accuracy of the proposed reconstruction method comparing with the conventional method.

TABLE II. Absolute permeability results of the five reconstructed pore structures obtained by numerical simulation using the fluid viscosity of ethanol.

		Direction	Absolute Permeability k (μm^2)
Simulation results	Model 1	X	1.31×10^{-6}
		Y	1.39×10^{-6}
		Z	1.19×10^{-6}
	Model 2	X	1.18×10^{-6}
		Y	1.15×10^{-6}
		Z	1.22×10^{-6}
	Model 3	X	1.24×10^{-6}
		Y	1.13×10^{-6}
		Z	1.58×10^{-6}
	Model 4	X	9.57×10^{-7}
		Y	1.06×10^{-6}
		Z	1.25×10^{-6}
	Model 5	X	1.15×10^{-6}
		Y	1.20×10^{-6}
		Z	1.33×10^{-6}
Experimental results	1.30×10^{-6} to 5.72×10^{-6} [79]		

D. Absolute permeability estimation

Permeability is a critical property of cementitious materials, which describes the ability of pore structures that allow fluid to flow through them. Absolute permeability describes the permeability of a porous medium when saturated with a single-phase fluid; it is an intrinsic property of materials and is only determined by the pore structures. Numerical methods such as a voxel-based solver and a pore network model can be used to estimate the absolute permeability from pore structures. Based on the literature, the pore network model simplifies the pore structures to spherical pore chambers and cylindrical pore throats, which can achieve higher computational speed. However, compared with a voxel-based solver, the simplification of the pore network model leads to less accuracy of the absolute permeability [76]. A voxel-based finite volume method was used in this work to estimate the absolute permeability using the reconstructed pore structures. AVIZO XLABSUITE EXTENSION software was used. The fluid was assumed to be incompressible and a Newtonian fluid, which meant density and dynamic viscosity were constant. The flow was assumed to be steady state and laminar flow, which meant the velocity did not change over time and no turbulence was produced. Four side faces of the model were assumed to be sealed and the no-slip boundary condition was applied on the interface. A pressure drop was applied to the two opposite faces to simulate the flow along one direction. A channel and a diverging part were added on the faces perpendicular to the main flow direction, which was used to stabilize the flow and ensured the spread of the flow on the input surface. Under the aforementioned assumptions and boundary conditions, the Stokes equation was simplified and solved, and Darcy's law was used to determine the absolute permeability.

Five models are reconstructed based on the same statistical correlation characterized from the 2D images. The input pressure of the simulation is 1.3×10^5 Pa and the output pressure is 1.0×10^5 Pa. The fluid viscosity μ is 1.082×10^{-3} Pa s, which is the dynamic viscosity of ethanol at 25° [77]. Ethanol as an organic liquid is believed to be chemically neutral compared to water and will cause the least damage to the microstructure of the cementitious materials; it can be assumed to be the absolute permeability which is only related to the pore structure [78]. The absolute permeabilities of the five reconstructed models are shown in Table II. The average absolute permeability of the five models is 1.22×10^{-6} μm^2; the standard deviation is $0.15 \times 10^{-6}\mu$m^2. As the standard deviation is about 12% of the averaged permeability, it indicates that the developed approach can construct 3D microstructures with statistically consistent properties. The experimentally measured ethanol permeability from the literature is 1.30×10^{-6} μm^2 to 5.72×10^{-6} μm^2 for different samples [79]. The numerically predicted permeability is close to the experimentally measured ethanol permeability. It should be noticed that the flow in this small scale has the potential to exhibit some slippage and may affect the accuracy of the results [80,81]. However, the slippage will not be further investigated here. The purpose of the permeability calculations is to demonstrate that the reconstructed 3D model can be used to predict material properties. The comprehensive prediction of permeability for heterogeneous materials such as cementitious materials needs further investigation on the representativity of the reconstructed models [82]. Instead of validating the prediction, the comparison between the prediction and the experimental results is used to confirm that the predicted results are reasonable.

The fluid flow in the pore structure of model 1 is visualized through the velocity field streamlines as shown in Fig. 11.

IV. CONCLUSIONS

A descriptor-based reconstruction method combined with a partition approach was proposed to reconstruct 3D microstructures based on a set of 2D SEM images. The descriptor-based method has the advantages of low-dimensional and high computational efficiency. The proposed partition approach extends the application of the

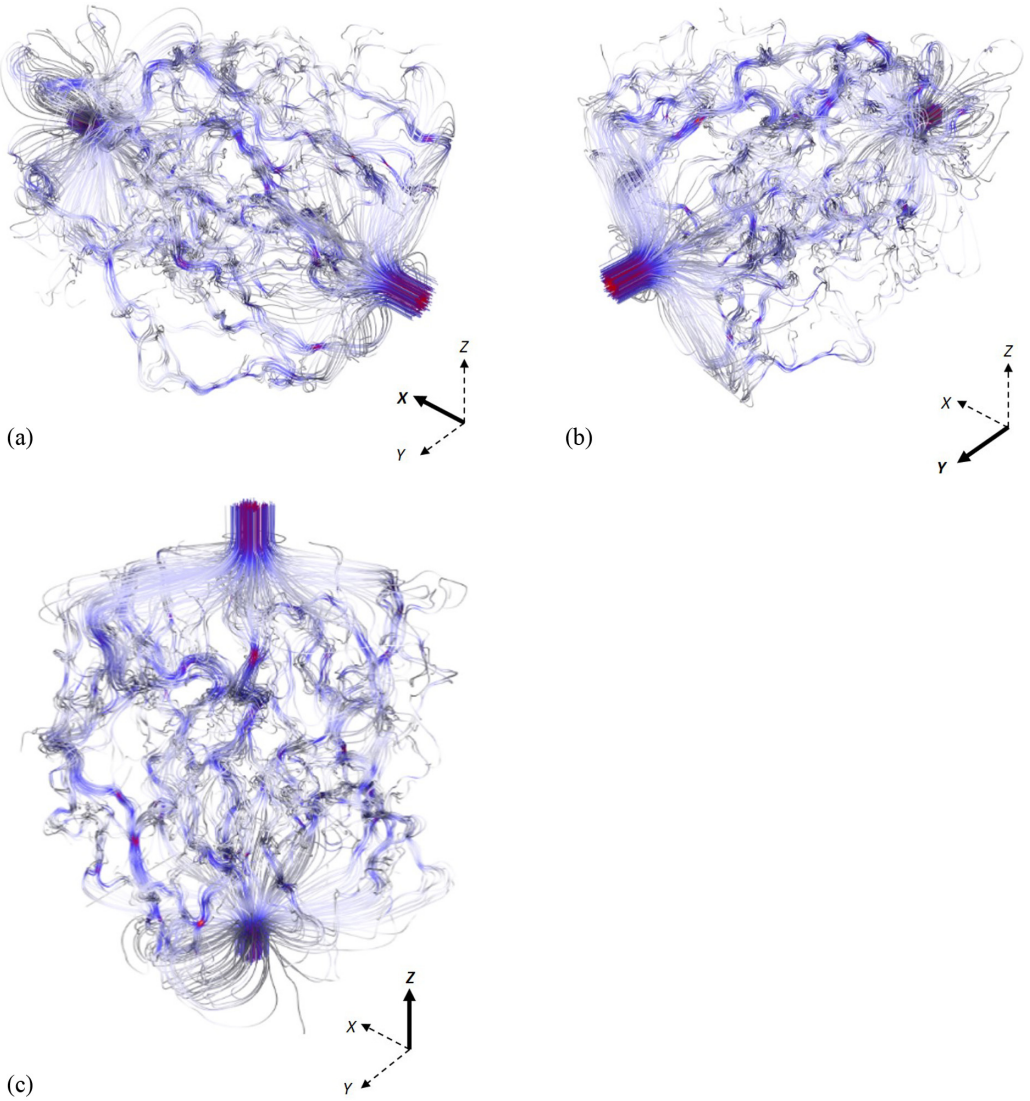

FIG. 11. Velocity field streamlines of fluid flow through the pore structure of model 1 from different directions: (a) *X* direction; (b) *Y* direction; (c) *Z* direction.

descriptor-based method to complex microstructures with features highly irregular and highly tortuous. The proposed partition approach uses the watershed algorithm to divide the irregular and connected features into small and regular partitioned features based on the gray-level gradient of the images and the roundness of the partitioned features. The partitioned features are characterized with the area fraction, size distribution, and spatial distribution. With stereological analysis, the 3D microstructure reconstruction based on information from the 2D images can be achieved for the complex microstructures. This enables the investigation of 3D features and properties of the microstructures, especially for the materials on the scales where only 2D images are available.

The proposed method was applied to reconstruct a 3D model from the 2D SEM images of the low-density CSH phase of a hardened cement paste. The comparisons between the original images and the reconstructed model cross sections showed an overall statistical equivalence with the pore descriptors. The statistical correlation functions of the reconstructed model cross sections agree well with the original images. The pores in the reconstructed 3D model are well connected and the shapes are highly irregular and tortuous. The absolute permeability was estimated from five reconstructed models using the voxel-based finite volume method. The numerically calculated absolute permeability results are close to the experimentally measured ethanol permeability of cementitious materials. This research provides a way to build the relationship between microstructures and properties directly and efficiently for material systems with complex microstructures, which can be further applied to optimize and design the microstructure based on the properties of the materials.

ACKNOWLEDGMENT

This research was supported by Australia Research Council through the Discovery Project (Grant No. DP160100119).

The authors declare no competing interests in this paper.

[1] R. Bostanabad, Y. Zhang, X. Li, T. Kearney, L. C. Brinson, D. W. Apley, W. K. Liu, and W. Chen, Prog. Mater Sci. **95**, 1 (2018).

[2] S. Torquato, Annu. Rev. Mater. Res. **40**, 101 (2010).

[3] L. M. Pant, S. K. Mitra, and M. Secanell, Phys. Rev. E **92**, 063303 (2015).

[4] C. L. Y. Yeong and S. Torquato, Phys. Rev. E **57**, 495 (1998).

[5] C. L. Y. Yeong and S. Torquato, Phys. Rev. E **58**, 224 (1998).

[6] C. Manwart, S. Torquato, and R. Hilfer, Phys. Rev. E **62**, 893 (2000).

[7] E.-Y. Guo, N. Chawla, T. Jing, S. Torquato, and Y. Jiao, Mater. Charact. **89**, 33 (2014).

[8] M. Sumanasooriya, D. Bentz, and N. Neithalath, ACI Mater. J. **107**, 413 (2010).

[9] S. Yu, Y. Zhang, C. Wang, W.-K. Lee, B. Dong, T. W. Odom, C. Sun, and W. Chen, J. Mech. Des. **139**, 071401 (2017).

[10] P. Čapek, V. Hejtmánek, L. Brabec, A. Zikánová, and M. Kočiřík, Transp. Porous Media **76**, 179 (2009).

[11] P. Čapek, V. Hejtmánek, J. Kolafa, and L. Brabec, Transp. Porous Media **88**, 87 (2011).

[12] T. Tang, Q. Teng, X. He, and D. Luo, J. Microsc. **234**, 262 (2009).

[13] L. M. Pant, S. K. Mitra, and M. Secanell, Phys. Rev. E **90**, 023306 (2014).

[14] M. V. Karsanina and K. M. Gerke, Phys. Rev. Lett. **121**, 265501 (2018).

[15] H. Xu, D. A. Dikin, C. Burkhart, and W. Chen, Comput. Mater. Sci. **85**, 206 (2014).

[16] H. Y. Xu, Y. Li, C. Brinson, and W. Chen, J. Mech. Des. **136**, 051007 (2014).

[17] R. Bostanabad, A. T. Bui, W. Xie, D. W. Apley, and W. Chen, Acta Mater. **103**, 89 (2016).

[18] J. Feng, Q. Teng, B. Li, X. He, H. Chen, and Y. Li, Comput. Methods Appl Mech. Eng. **368**, 113043 (2020).

[19] G. Coiffier, P. Renard, and S. Lefebvre, Front. Water **2**, 560598 (2020).

[20] W. Pabst, E. Gregorová, and T. Uhlířová, Mater. Charact. **105**, 1 (2015).

[21] A. P. Roberts and E. J. Garboczi, J. Mech. Phys. Solids **50**, 33 (2002).

[22] J. Randrianalisoa, D. Baillis, C. L. Martin, and R. Dendievel, Int. J. Therm. Sci. **98**, 277 (2015).

[23] T. Steriotis, E. Kikkinides, M. Kainourgiakis, A. Stubos, and J. D. F. Ramsay, Colloids Surf. A **241**, 231 (2004).

[24] C. S. Stiapis, E. D. Skouras, and V. N. Burganos, Materials **12**, 4085 (2019).

[25] J. F. Thovert and P. M. Adler, Phys. Rev. E **83**, 056116 (2011).

[26] J. F. Thovert, F. Yousefian, P. Spanne, C. G. Jacquin, and P. M. Adler, Phys. Rev. E **63**, 061307 (2001).

[27] M. G. Politis, E. S. Kikkinides, M. E. Kainourgiakis, and A. K. Stubos, Microporous Mesoporous Mater. **110**, 92 (2008).

[28] K. K. Aligizaki, *Pore Structure of Cement-Based Materials: Testing, Interpretation and Requirements* (CRC Press, Boca Raton, FL, 2006).

[29] P. K. A. Mehta and P. K. Mehta, in *Concrete: Microstructure, Properties, and Materials*, 4th ed., edited by P. K. Mehta and P. J. M. Monteiro (McGraw-Hill Education, New York, 2014).

[30] D. Hou, D. Li, P. Hua, J. Jiang, and G. Zhang, Cem. Concr. Compos. **96**, 11 (2019).

[31] H. Du and S. D. Pang, Cem. Concr. Res. **76**, 10 (2015).

[32] S. J. Chen, W. G. Li, C. K. Ruan, K. Sagoe-Crentsil, and W. H. Duan, Constr. Build. Mater. **154**, 95 (2017).

[33] W. Wang, S. J. Chen, F. Basquiroto De Souza, B. Wu, and W. H. Duan, Nanoscale **10**, 1004 (2018).

[34] F. U. A. Shaikh and S. W. M. Supit, Constr. Build. Mater. **99**, 208 (2015).

[35] H. Chen, P. Feng, Y. Du, J. Jiang, and W. Sun, Constr. Build. Mater. **182**, 620 (2018).

[36] H. Du, S. Du, and X. Liu, Constr. Build. Mater. **73**, 705 (2014).

[37] E. Ghafari, H. Costa, E. Júlio, A. Portugal, and L. Durães, Mater. Des. **59**, 1 (2014).

[38] A. Joshaghani, M. Balapour, M. Mashhadian, and T. Ozbakkaloglu, Constr. Build. Mater. **245**, 118444 (2020).

[39] R. Liu, H. Xiao, H. Li, L. Sun, Z. Pi, G. Waqar, T. Du, and L. Yu, J. Mater. Sci. Lett. **53**, 4974 (2018).

[40] S. Chuah, Z. Pan, J. G. Sanjayan, C. M. Wang, and W. H. Duan, Constr. Build. Mater. **73**, 113 (2014).

[41] A. Mohammed, J. G. Sanjayan, W. H. Duan, and A. Nazari, Constr. Build. Mater. **84**, 341 (2015).

[42] Z. Pan, L. He, L. Qiu, A. H. Korayem, G. Li, J. W. Zhu, F. Collins, D. Li, W. H. Duan, and M. C. Wang, Cem. Concr. Compos. **58**, 140 (2015).

[43] S. Jin, J. Zhang, and S. Han, Constr. Build. Mater. **135**, 1 (2017).

[44] S. Diamond, Cem. Concr. Res. **30**, 1517 (2000).

[45] S.-Y. Chung, T.-S. Han, and S.-Y. Kim, Constr. Build. Mater. **87**, 45 (2015).

[46] E. Gallucci, K. Scrivener, A. Groso, M. Stampanoni, and G. Margaritondo, Cem. Concr. Res. **37**, 360 (2007).

[47] M. Zhang and A. P. Jivkov, Composites, Part B **88**, 64 (2016).

[48] S. Xue, P. Zhang, J. Bao, L. He, Y. Hu, and S. Yang, Mater. Charact. **160**, 110085 (2020).

[49] J.-S. Kim, S.-Y. Chung, D. Stephan, and T.-S. Han, Constr. Build. Mater. **202**, 82 (2019).

[50] Y. Song, C. A. Davy, D. Troadec, and X. Bourbon, Cem. Concr. Res. **115**, 308 (2019).

[51] S. Lim, H.-S. Lee, and S. Kawashima, Mater. Charact. **145**, 323 (2018).

[52] K. M. Gerke, E. V. Korostilev, K. A. Romanenko, and M. V. Karsanina, Geoderma **383**, 114739 (2021).

[53] S. J. Chen, Y. Tian, C. Y. Li, and W. H. Duan, Geomech Geophys. Geo-Energy Geo-Resour. **2**, 173 (2016).

[54] G. Requena, G. Fiedler, B. Seiser, P. Degischer, M. Di Michiel, and T. Buslaps, Composites, Part A **40**, 152 (2009).

[55] J. Wu, Y. Yuan, H. Gong, and T. L. Tseng, IISE Trans. **50**, 570 (2018).

[56] J. Schindelin, I. Arganda-Carreras, E. Frise, V. Kaynig, M. Longair, T. Pietzsch, S. Preibisch, C. Rueden, S. Saalfeld, B. Schmid *et al.*, Nat. Methods **9**, 676 (2012).

[57] T. W. Ridler and S. Calvard, IEEE Trans. Syst. Man Cybern. **8**, 630 (1978).

[58] P. Soille and L. M. Vincent, Proc. SPIE: Visual Commun. Image Proces. **1360**, 240 (1990).

[59] P. Wang, H. Lei, X. Zhu, H. Chen, and D. Fang, Int. J. Heat Mass Transfer **144**, 118632 (2019).

[60] D. Westhoff, T. Danner, S. Hein, R. Scurtu, L. Kremer, A. Hoffmann, A. Hilger, I. Manke, M. Wohlfahrt-Mehrens, A. Latz *et al.*, Mater. Charact. **151**, 166 (2019).

[61] Q. Xu, W. Long, H. Jiang, B. Ma, C. Zan, D. Ma, and L. Shi, Chem. Eng. J. **331**, 856 (2018).
[62] S. A. Saltykov, *Stereometric Metallography*, 2nd ed. (State Publishing House for Metals and Science, Moscow, 1958).
[63] E. R. Weibel, *Stereological Methods* (Academic Press, London, 1979).
[64] H. Shen, S. M. Oppenheimer, D. C. Dunand, and L. C. Brinson, Mech. Mater. **38**, 933 (2006).
[65] T. Li, S. Shimasak, S. Taniguchi, and S. Narita, ISIJ Int. **56**, 1625 (2016).
[66] S. Torquato, *Random Heterogeneous Materials: Microstructure and Macroscopic Properties* (Springer, New York, 2002).
[67] M. D. Rintoul and S. Torquato, J. Colloid Interface Sci. **186**, 467 (1997).
[68] M. L. Larsen and R. A. Shaw, Atmos. Meas. Tech. **11**, 4261 (2018).
[69] X.-S. Yang, *Nature-Inspired Optimization Algorithms*, 1st ed. (Elsevier, London, 2014).
[70] X. Miao, K. M. Gerke, and T. O. Sizonenko, Adv. Water Res. **105**, 162 (2017).
[71] N. Jamil, Z. A. Bakar, and T. M. T. Sembok, in *Geometric Modeling and Imaging—New Trends (GMAI '06)* (IEEE, Piscataway, NJ, 2006), pp. 171–176.
[72] M. V. Karsanina, K. M. Gerke, E. B. Skvortsova, and D. Mallants, PLoS ONE **10**, e0126515 (2015).
[73] E. B. Skvortsova, Eurasian Soil Sci. **42**, 1254 (2009).
[74] Y. Jiao, F. H. Stillinger, and S. Torquato, Phys. Rev. **76**, 031110 (2007).
[75] B. Lu and S. Torquato, Phys. Rev. A **45**, 7292 (1992).
[76] R. Song, Y. Wang, J. Liu, M. Cui, and Y. Lei, Energy Sci. Eng. **7**, 2842 (2019).
[77] B. González, A. Domínguez, and J. Tojo, J. Chem. Eng. Data **49**, 1590 (2004).
[78] H. Loosveldt, Z. Lafhaj, and F. Skoczylas, Cem. Concr. Res. **32**, 1357 (2002).
[79] C. Zhou, W. Chen, W. Wang, and F. Skoczylas, Cem. Concr. Res. **82**, 117 (2016).
[80] Y. Song, G. Dai, L. Zhao, Z. Bian, P. Li, and L. Song, Constr. Build. Mater. **247**, 118527 (2020).
[81] A. Afsharpoor and F. Javadpour, Fuel **180**, 580 (2016).
[82] K. M. Gerke and M. V. Karsanina, Eur. J. Soil Sci. **72**, 527 (2021).